Journal of Science and Transport Technology
Journal homepage: https://jstt.vn/index.php/en

UNIVERSITY OF TRANSPORT TECHNOLOGY

Article info
Type of article:
Original research paper

DOI:
https://doi.org/10.58845/jstt.utt.2026.en.6.4.130-143

*Corresponding author:
Email address:
tttruong@hcmut.edu.vn

Received: 06/12/2025
Received in Revised Form: 15/03/2026
Accepted: 27/05/2026

A Meshfree Proportional Topology Optimization of Bi-Directional Functionally Graded Plates Based on Third-Order Shear Deformation Theory

Vay Siu Lo[1, 2], Thien Tich Truong[1, 2,*]

[1] Department of Engineering Mechanics, Faculty of Applied Science, Ho Chi Minh City University of Technology (HCMUT), 268 Ly Thuong Kiet Street, Dien Hong Ward, Ho Chi Minh City, Viet Nam

[2] Vietnam National University Ho Chi Minh City, Vo Truong Toan Street, VNU-HCM Urban Area, Quarter 33, Linh Xuan Ward, Ho Chi Minh City, Viet Nam

Abstract: This work develops a meshfree topology optimization formulation for plates composed of bidirectional functionally graded materials (2D-FGM). The plate response is described using the third-order shear deformation theory, allowing transverse shear effects to be incorporated without shear correction factors. The radial point interpolation method (RPIM) is adopted to construct the approximation field, thereby reducing the reliance on conventional mesh-based discretization. The spatial variation of material properties in the two in-plane directions is defined through a power-law model. For topology optimization, a proportional topology optimization (PTO) strategy is employed to iteratively redistribute material according to the structural response without requiring sensitivity gradients. Several numerical studies are carried out to assess the performance of the proposed approach. The results indicate that the present formulation can produce stiff and smooth material layouts for 2D-FGM plates. The proposed RPIM-PTO framework therefore provides an effective computational tool for the lightweight design of advanced graded plate structures.

Keywords: Functionally graded plates; Meshfree method; PTO; RPIM; Topology optimization; Third-order shear deformation theory.

1. Introduction

Topology optimization (TO) is a computational design technique aimed at determining the optimal material distribution within a prescribed design domain to maximize structural performance under given loading and boundary conditions. A variety of numerical strategies have been proposed for TO, notably the solid isotropic material with penalization (SIMP) method [1], the evolutionary structural optimization (ESO) method [2], the level set method [3], and the phase-field method [4].

Conventional TO approaches typically rely on gradient-based optimization, which necessitates the computation of sensitivity information, i.e., the derivatives of the objective and constraint functions with respect to design variables [5]. As an alternative, gradient-free techniques such as the proportional topology optimization (PTO) method have been developed

[6]. PTO achieves material redistribution by proportionally assigning material based on strain energy, thereby avoiding the complexity of sensitivity analysis and enhancing computational efficiency.

While traditional TO frameworks predominantly use mesh-based finite element methods (FEM), meshfree methods have emerged as powerful alternatives due to their flexibility in handling complex geometries and high-order approximation capabilities. Among meshfree formulations, the radial point interpolation method (RPIM) [7] stands out for its Kronecker delta property, which simplifies the enforcement of essential boundary conditions. RPIM also facilitates high-order continuity, making it particularly suitable for problems involving higher-order theories. The integration of meshfree methods into topology optimization has gained increasing interest in recent years [8, 9].

Recent advancements have extended TO to plate and shell structures, which are widely utilized in aerospace, civil, and mechanical engineering applications due to their high strength-to-weight ratio. The use of plate theories, such as classical plate theory [10], first-order shear deformation theory [11], and higher-order shear deformation theories (HSDT) [12], reduces computational cost compared to full 3D solid modeling. Among HSDTs, the third-order shear deformation theory (TSDT) has received particular attention due to its ability to capture cross-sectional warping and provide accurate stress and displacement predictions, especially for thick plates. In the context of TO, employing a higher-order theory like TSDT is essential to ensure that the computed structural responses, such as compliance, accurately reflect the real behavior of the system.

Recent studies have further expanded the design and optimization of functionally graded plate structures. In particular, bi-directional functionally graded plates have attracted increasing attention because their spatially varying material distributions offer greater flexibility for tailoring stiffness and structural response [13, 14]. Representative recent works have addressed both the optimization of bi-directional graded plates and the design of advanced graded porous structures [15]. In parallel, meshfree and direct meshfree topology optimization methods have developed rapidly, including maximum-entropy-based meshless proportional topology optimization, stress-based meshfree topology optimization, and direct meshfree topology optimization using neural-network approximations [16, 17]. On the analysis side, refined higher-order shear deformation theories have also been proposed for functionally graded plates to more accurately capture transverse shear effects and stress fields [18]. Motivated by these developments, the present study develops a meshfree topology optimization framework that combines RPIM, PTO, and TSDT for bi-directional functionally graded plates.

This study develops a meshfree topology optimization framework for plates made from bi-directional functionally graded materials (2D-FGMs), combining TSDT, RPIM, and the PTO algorithm. While TSDT requires second-order derivatives, making it incompatible with low-order finite elements, the high-order shape functions inherent to RPIM naturally accommodate this requirement. Furthermore, the PTO algorithm is adapted for use in a meshfree context by defining pseudo-densities at RPIM integration points, allowing for a high-resolution material distribution. This study is particularly beneficial in cases involving complex material distributions, such as those found in 2D-FGMs, where the elastic properties vary along both in-plane directions.

The structure of this paper is as follows: Section 2 describes the implementation of the PTO algorithm. Section 3 details the formulation of TSDT and the model of the bi-directional functionally graded material. The validation of the current approach is presented in Section 4. Section 5 presents numerical examples that demonstrate the performance of the method under various material gradation scenarios. Section 6 concludes the study and outlines potential directions for future research.

2. The Proportional Topology Optimization

The topology optimization problem for minimizing the compliance of structures is mathematically formulated as follows, subject to equilibrium and volume constraints [19]:

$$\begin{aligned} &\text{minimize} && c = \mathbf{u}^{T}\mathbf{K}(\rho)\mathbf{u} \\ &\text{subject to} && \int_{\Omega} \rho \, d\Omega \le f|\Omega|,\ \rho \in [0,1] \\ & && \mathbf{K}(\rho)\mathbf{u} = \mathbf{F} \end{aligned} \quad (1)$$

Fundamentally, the compliance c in Eq. (1) corresponds to twice the total strain energy of the system, and it can be evaluated upon obtaining the displacement field $\mathbf{u}$ by solving the equilibrium equations. The design variable (pseudo-density) ρ is used to depict material distribution, where ρ=0 indicates a void and ρ=1 indicates a fully solid. The constraint expressed in Eq. (1) enforces that the material volume of the optimized structure does not exceed a prescribed volume fraction f of the total design domain.

In this study, since the RPIM meshfree method is employed as the main numerical method for solving structural behavior, the design variables ρ are specified at integration points. The elastic modulus at each integration point i is interpolated using the solid isotropic material with penalization scheme [5], defined as follows:

$$E_i = E_{void} + \rho_i^p (E_0 - E_{void}) \quad (2)$$

where p is the penalization power. The Young's modulus of the solid material is denoted as E_0, while E_{void} is assigned a very small value to ensure the stiffness is non-zero when ρ_i=0.

By evaluating the compliance at each integration point, the pseudo-density field is iteratively updated within an inner optimization loop according to the following scheme [6, 19, 20]:

$$\rho_i = RM \frac{k c_i}{\sum_{j=1}^{n} c_j} \quad (3)$$

where k controls the rate of material redistribution during the iterative process, while RM denotes the remaining material volume. At the beginning of each inner iteration loop, RM is initialized to the target material amount. The loop proceeds until the remaining material drops below a prescribed tolerance threshold, typically $RM \le 10^{-4}$.

The compliance c_i at the integration point is defined as follows [19]:

$$c_i = \mathbf{u}_{Si}^{T}\mathbf{K}_i\mathbf{u}_{Si} \quad (4)$$

where $\mathbf{u}_{Si}$ is the vector of nodal displacements in the support domain S_i of integration point i.

Upon completion of the inner loop, the pseudo densities are revised to incorporate the redistributed material configuration based on the evaluated structural response [6]:

$$\rho_{t+1} = \alpha\rho_t + (1-\alpha)\rho_{new} \quad (5)$$

where ρ_t is the value of density from the previous iteration, and ρ_{new} indicates the newly obtained value after the inner loop process. $\alpha \in [0, 1]$ determining the proportion between ρ_t and ρ_{new} in computing the value of the current density ρ_{t+1}. In this study, α = 0.5 is chosen.

The essential idea of PTO is to interpret the compliance distribution as an indicator of the relative structural importance of different regions in the design domain. Regions with higher local compliance contribution are assigned more material in the subsequent iteration, whereas regions with lower contribution receive less material. Therefore, the algorithm performs material redistribution according to structural demand rather than through the explicit evaluation of objective-function derivatives. This is the key difference between PTO and traditional sensitivity-based topology optimization methods such as SIMP combined with OC or MMA schemes.

For the present RPIM-based formulation, this feature is particularly useful because the pseudo-density variables are associated with integration points, leading to a fine spatial description of the material field. In such a meshfree context, PTO provides a convenient update strategy that avoids the additional complexity of deriving and implementing sensitivities with respect to a large number of integration-point design variables. Moreover, the relaxation step introduced in Eq. (5) helps prevent abrupt changes in the density field between successive iterations, thereby improving numerical stability and promoting a smoother optimization history.

3. Third-order shear deformation theory

3.1. Kinematics and constitutive equation

According to the third-order shear deformation theory [21], the displacement field of the plate can be represented by the following formulation:

$$\begin{aligned} u(x,y,z) &= u_0(x,y) + z\phi_x - \frac{4}{3h^2} z^3\left(\phi_x + \frac{\partial w_0}{\partial x}\right) \\ v(x,y,z) &= v_0(x,y) + z\phi_y - \frac{4}{3h^2} z^3\left(\phi_y + \frac{\partial w_0}{\partial y}\right) \\ w(x,y,z) &= w_0(x,y) \end{aligned} \quad (6)$$

where u_0, v_0, w_0 denote the displacements of a point on the mid-surface of the plate along the x-, y-, and z-axes, respectively. The notations ϕ_x and ϕ_y represent the rotations of the normal to the mid-surface about the y- and x-axes, respectively. Fig. 1 shows the sign convention of the above 5 degrees of freedom. The thickness of the plate is denoted by the letter h.

The linear strain is obtained from Eq. (6) as follows:

$$\boldsymbol{\varepsilon} = \begin{bmatrix} \boldsymbol{\varepsilon}_0 \\ \mathbf{0} \end{bmatrix} + \begin{bmatrix} z\boldsymbol{\kappa}_{b0} \\ \boldsymbol{\varepsilon}_s \end{bmatrix} + \begin{bmatrix} z^3\boldsymbol{\kappa}_{b2} \\ z^2\boldsymbol{\kappa}_{s2} \end{bmatrix} \quad (7)$$

where $\boldsymbol{\varepsilon}_0$, $\boldsymbol{\kappa}_{b0}$, $\boldsymbol{\varepsilon}_s$, $\boldsymbol{\kappa}_{b2}$ and $\boldsymbol{\kappa}_{s2}$, in sequence, represent the in-plane membrane strains, classical bending strains, transverse shear strains, bending strains involving second-order derivatives of displacement, and shear strains linked to the second-order variation with respect to the thickness coordinate z. Particularly,

$$\begin{aligned} &\boldsymbol{\varepsilon}_0 = \left[\frac{\partial u_0}{\partial x} \quad \frac{\partial v_0}{\partial y} \quad \left(\frac{\partial u_0}{\partial y} + \frac{\partial v_0}{\partial x}\right)\right]^T, \; \boldsymbol{\kappa}_{b0} = \left[\frac{\partial \phi_x}{\partial x} \quad \frac{\partial \phi_y}{\partial y} \quad \left(\frac{\partial \phi_x}{\partial y} + \frac{\partial \phi_y}{\partial x}\right)\right]^T, \; \boldsymbol{\varepsilon}_s = \left[\left(\frac{\partial w_0}{\partial x} + \phi_x\right) \quad \left(\frac{\partial w_0}{\partial y} + \phi_y\right)\right]^T, \\ &\boldsymbol{\kappa}_{s2} = \left[\left(\frac{\partial w_0}{\partial x} + \phi_x\right) \quad \left(\frac{\partial w_0}{\partial y} + \phi_y\right)\right]^T, \; \boldsymbol{\kappa}_{b2} = \left[\left(\frac{\partial^2 w_0}{\partial x^2} + \frac{\partial \phi_x}{\partial x}\right) \quad \left(\frac{\partial^2 w_0}{\partial y^2} + \frac{\partial \phi_y}{\partial y}\right) \quad \left(2\frac{\partial^2 w_0}{\partial x \partial y} + \frac{\partial \phi_x}{\partial y} + \frac{\partial \phi_y}{\partial x}\right)\right]^T \end{aligned} \quad (8)$$

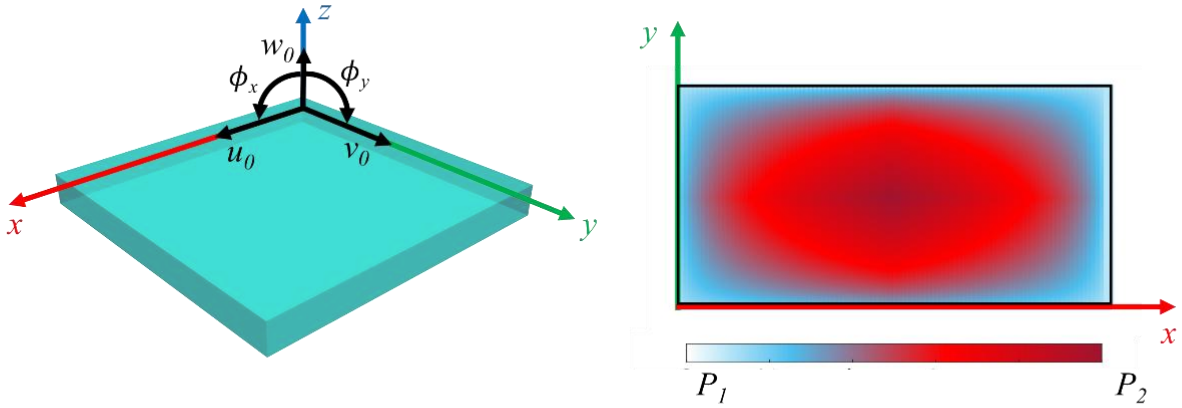

Fig. 1. Degrees of freedom of the TSDT plate (left) and the distribution of material phase in bi-directional FGM (right).

The constitutive equation is determined as the following relation

$$\underset{[13\times1]}{\hat{\boldsymbol{\sigma}}} = \begin{bmatrix} \mathbf{N} \\ \mathbf{M} \\ \mathbf{P} \\ \mathbf{Q} \\ \mathbf{R} \end{bmatrix} = \begin{bmatrix} \mathbf{A} & \mathbf{B} & \mathbf{E} & \mathbf{0} & \mathbf{0} \\ \mathbf{B} & \mathbf{D} & \mathbf{G} & \mathbf{0} & \mathbf{0} \\ \mathbf{E} & \mathbf{G} & \mathbf{H} & \mathbf{0} & \mathbf{0} \\ \mathbf{0} & \mathbf{0} & \mathbf{0} & \mathbf{A} & \mathbf{D} \\ \mathbf{0} & \mathbf{0} & \mathbf{0} & \mathbf{D} & \mathbf{G} \end{bmatrix} \begin{bmatrix} \boldsymbol{\varepsilon}_0 \\ \boldsymbol{\kappa}_{b0} \\ \boldsymbol{\kappa}_{b2} \\ \boldsymbol{\varepsilon}_s \\ \boldsymbol{\kappa}_{s2} \end{bmatrix} = \underset{[13\times13]}{\hat{\mathbf{C}}} \underset{[13\times1]}{\hat{\boldsymbol{\varepsilon}}} \quad (9)$$

where $\mathbf{N}$ is the in-plane force resultants, $\mathbf{M}$ is the moment resultants, $\mathbf{Q}$ is shear force resultants, $\mathbf{P}$ and $\mathbf{R}$ are higher-order resultants. They are defined as

$$\begin{aligned} \mathbf{N} &= \begin{bmatrix} N_{xx} \\ N_{yy} \\ N_{xy} \end{bmatrix} = \int_{-h/2}^{h/2} \begin{bmatrix} \sigma_{xx} \\ \sigma_{yy} \\ \sigma_{xy} \end{bmatrix} dz, \\ \mathbf{M} &= \begin{bmatrix} M_{xx} \\ M_{yy} \\ M_{xy} \end{bmatrix} = \int_{-h/2}^{h/2} \begin{bmatrix} \sigma_{xx} \\ \sigma_{yy} \\ \sigma_{xy} \end{bmatrix} z dz, \end{aligned} \quad (10)$$

$$\mathbf{P} = \begin{bmatrix} P_{xx} \\ P_{yy} \\ P_{xy} \end{bmatrix} = \int_{-h/2}^{h/2} \begin{bmatrix} \sigma_{xx} \\ \sigma_{yy} \\ \sigma_{xy} \end{bmatrix} z^3 \mathrm{d}z,$$

$$\mathbf{Q} = \begin{bmatrix} Q_x \\ Q_y \end{bmatrix} = \int_{-h/2}^{h/2} \begin{bmatrix} \sigma_{xz} \\ \sigma_{yz} \end{bmatrix} \mathrm{d}z,$$

$$\mathbf{R} = \begin{bmatrix} R_x \\ R_y \end{bmatrix} = \int_{-h/2}^{h/2} \begin{bmatrix} \sigma_{xz} \\ \sigma_{yz} \end{bmatrix} z^2 \mathrm{d}z$$

and the matrices **A**, **B**, **D**, **E**, **G** and **H** in Eq. (9) are defined as follows

$$\left(A_{ij}, B_{ij}, D_{ij}, E_{ij}, G_{ij}, H_{ij}\right) = \int_{-h/2}^{h/2} Q_{ij}\left(1, z, z^2, z^3, z^4, z^6\right) \mathrm{d}z \tag{11}$$

in which the stiffnesses A_{ij}, D_{ij}, and G_{ij} are defined for i, j = 1, 2, 4, 5, 6 while the stiffnesses B_{ij}, E_{ij}, and H_{ij} are only defined for i, j = 1, 2, 6. The reduced elastic coefficients are given as

$$Q_{11} = Q_{22} = \frac{E}{1-v^2},$$
$$Q_{12} = \frac{vE}{1-v^2}, \tag{12}$$
$$Q_{44} = Q_{55} = Q_{66} = \frac{E}{2(1+v)}$$

where v is Poisson's ratio. Other Q_{ij} values, not mentioned above, have a value of zero.

The plate is composed of two distinct material constituents, whose volume fractions vary smoothly along the in-plane directions, as illustrated in Fig. 1. This spatial gradation leads to an effective Young's modulus $E(x,y)$ that is position-dependent and can be evaluated using the rule of mixtures

$$E(x,y) = (E_2 - E_1)\, V_x V_y + E_1 \tag{13}$$

where E_1 and E_2 denote the Young's modulus of the two constituent phases, while V_x and V_y represent their corresponding volume fractions along the in-plane directions. It is assumed that the spatial distribution of these volume fractions in the bidirectional functionally graded material plate follows a power-law function

$$\begin{cases} V_x = \begin{cases} \left(2\dfrac{x}{L_x}\right)^{m_x} & 0 \le x \le 0.5L_x \\ \left(2\text{-}2\dfrac{x}{L_x}\right)^{m_x} & 0.5L_x \le x \le L_x \end{cases} \\ V_y = \begin{cases} \left(2\dfrac{y}{L_y}\right)^{m_y} & 0 \le y \le 0.5L_y \\ \left(2\text{-}2\dfrac{y}{L_y}\right)^{m_y} & 0.5L_y \le y \le L_y \end{cases} \end{cases} \tag{14}$$

in which, m_x and m_y are the material gradient indexes in x and y directions, respectively.

3.2. Meshfree discrete formulations

In this study, the shape function ψ_i is formulated using the meshfree radial point interpolation method. For a detailed exposition of the construction procedure, the reader is referred to [7]. Briefly, the RPIM shape function consists of two components: a radial basis function and a polynomial basis function. In this work, a quartic radial basis function is employed to construct the interpolation function [11], as detailed below

$$R(\mathbf{x}_i,\mathbf{x}_j) = 1\text{-}6\left(\frac{\theta}{l_s}\right)^2 r_{ij}^2 + 8\left(\frac{\theta}{l_s}\right)^3 r_{ij}^3 - 3\left(\frac{\theta}{l_s}\right)^4 r_{ij}^4 \tag{15}$$

where $r_{ij} = \|\mathbf{x}_i\text{-}\mathbf{x}_j\|$, θ is the shape parameter, and l_s is the largest distance between any pair of nodes inside the support domain. The stiffness matrix is defined as follows:

$$\mathbf{K} = \int_\Omega \mathbf{B}^T \hat{\mathbf{C}} \mathbf{B} \mathrm{d}\Omega \tag{16}$$

where $\mathbf{B}_i$ is the strain computing matrix and expressed as

$$\underset{[13\times5]}{\mathbf{B}_i} = \left[\left(\mathbf{B}_i^0\right)^T \quad \left(\mathbf{B}_i^{b0}\right)^T \quad \left(\mathbf{B}_i^{b2}\right)^T \quad \left(\mathbf{B}_i^{s}\right)^T \quad \left(\mathbf{B}_i^{s2}\right)^T \right]^T \tag{17}$$

in which

$$\underset{[3\times5]}{\mathbf{B}_i^0} = \begin{bmatrix} \dfrac{\partial\psi_i}{\partial x} & 0 & 0 & 0 & 0 \\ 0 & \dfrac{\partial\psi_i}{\partial y} & 0 & 0 & 0 \\ \dfrac{\partial\psi_i}{\partial y} & \dfrac{\partial\psi_i}{\partial x} & 0 & 0 & 0 \end{bmatrix} \tag{18}$$

$$\mathbf{B}_{\substack{\mathrm{i}\\ [3\times5]}}^{\mathrm{b0}} = \begin{bmatrix} 0 & 0 & 0 & \frac{\partial\psi_i}{\partial x} & 0 \\ 0 & 0 & 0 & 0 & \frac{\partial\psi_i}{\partial y} \\ 0 & 0 & 0 & \frac{\partial\psi_i}{\partial y} & \frac{\partial\psi_i}{\partial x} \end{bmatrix}$$

$$\mathbf{B}_{\substack{\mathrm{i}\\ [3\times5]}}^{\mathrm{b2}} = -\frac{4}{3h^2}\begin{bmatrix} 0 & 0 & \frac{\partial^2\psi_i}{\partial x^2} & \frac{\partial\psi_i}{\partial x} & 0 \\ 0 & 0 & \frac{\partial^2\psi_i}{\partial y^2} & 0 & \frac{\partial\psi_i}{\partial y} \\ 0 & 0 & 2\frac{\partial^2\psi_i}{\partial x\partial y} & \frac{\partial\psi_i}{\partial y} & \frac{\partial\psi_i}{\partial x} \end{bmatrix}$$

$$\mathbf{B}_{\substack{\mathrm{i}\\ [2\times5]}}^{\mathrm{s}} = \begin{bmatrix} 0 & 0 & \frac{\partial\psi_i}{\partial x} & \psi_i & 0 \\ 0 & 0 & \frac{\partial\psi_i}{\partial y} & 0 & \psi_i \end{bmatrix}$$

$$\mathbf{B}_{\substack{\mathrm{i}\\ [2\times5]}}^{\mathrm{s2}} = -\frac{4}{h^2}\begin{bmatrix} 0 & 0 & \frac{\partial\psi_i}{\partial x} & \psi_i & 0 \\ 0 & 0 & \frac{\partial\psi_i}{\partial y} & 0 & \psi_i \end{bmatrix}$$

And for the modal analysis, the mass matrix is defined as follows:

$$\mathbf{M} = \int_{\Omega} \mathbf{\Psi}^{\mathrm{T}}\mathbf{I}\mathbf{\Psi}\mathrm{d}\Omega \tag{19}$$

where

$$\mathbf{\Psi} = \begin{bmatrix} \psi_i & 0 & 0 & 0 & 0 \\ 0 & \psi_i & 0 & 0 & 0 \\ 0 & 0 & \psi_i & 0 & 0 \\ 0 & 0 & 0 & \psi_i & 0 \\ 0 & 0 & 0 & 0 & \psi_i \end{bmatrix} \tag{20}$$

and

$$\mathbf{I} = \rho\begin{bmatrix} h & 0 & 0 & 0 & 0 \\ 0 & h & 0 & 0 & 0 \\ 0 & 0 & h & 0 & 0 \\ 0 & 0 & 0 & \frac{h^3}{12} & 0 \\ 0 & 0 & 0 & 0 & \frac{h^3}{12} \end{bmatrix} \tag{21}$$

in which ρ is the density.

4. Validation of the current approach

4.1. Free vibration analysis of 2D-FGM plate

Before presenting the topology optimization results for bi-directional functionally graded plates, the accuracy of the underlying TSDT-RPIM solver is first examined through a benchmark problem. The objective of this example is to verify the structural analysis component of the present formulation independently of the optimization procedure. For this purpose, the plate natural frequencies predicted by the present approach are compared with analytical solutions available in the literature.

In this example, numerical results are presented to investigate the vibration characteristics of 2D-FGM plates. For the computation, the plate is assumed to consist of two constituent materials, namely metal (Al) and ceramic (SiC). Their material properties are taken as follows: for Al, E_1 = 71 GPa, ρ_1 = 2780 kg/m^3, and v_1 = 0.3; for SiC, E_2 = 427 GPa, ρ_2 = 3100 kg/m^3, and v_2 = 0.17. The square plate has a side length of a = 1 m and a thickness ratio of a/h = 100. The results are expressed in dimensionless form throughout the following analysis:

$$\bar{\omega} = \omega a^2\sqrt{\frac{\rho_2 h}{D}},\quad D = \frac{E_2 h^3}{12(1-v_2^2)} \tag{22}$$

A discretized model consisting of 15×15 nodes is employed. The shape functions are constructed using the radial point interpolation method, while the third-order shear deformation theory is adopted for plate modeling. The results obtained in the present study are compared with the semi-analytical solution reported in Ref. [22].

Table 1 presents the non-dimensional first-mode frequency of a square plate with all four edges clamped (CCCC) for different values of the gradation indices m_x and m_y. Table 2 reports the corresponding non-dimensional first-mode frequency of a square plate with all four edges simply supported (SSSS) for various combinations of m_x and m_y. As shown in these tables, the results of the present study are in good agreement with the semi-analytical solution in Ref. [22], thereby confirming the accuracy and validity of the proposed method and computational model.

However, it should be noted that the discrepancies in the SSSS cases are noticeably larger than those observed for the CCCC cases.

The obtained agreement in terms of natural frequencies confirms that the structural analysis core of the current approach is reliable. This provides a sound basis for its subsequent use in the topology optimization framework developed in this study.

Table 1. Non-dimensional mode 1 frequency of the CCCC 2D-FGM plate.

m_x	0.3			0.5			1			2			5		
m_y	Ref. [22]	Present	% Diff.	Ref. [22]	Present	% Diff.	Ref. [22]	Present	% Diff.	Ref. [22]	Present	% Diff.	Ref. [22]	Present	% Diff.
0.3	29.4893	29.611	0.41	27.9933	28.1087	0.41	25.5574	25.6495	0.36	23.1356	23.124	0.05	20.2241	20.0437	0.89
0.5	27.9936	28.1087	0.41	26.6024	26.7577	0.58	24.3786	24.5333	0.63	22.2299	22.2645	0.16	19.6778	19.5228	0.79
1	25.5573	25.6495	0.36	24.379	24.5333	0.63	22.5588	22.7147	0.69	20.881	20.9052	0.12	18.9031	18.739	0.87
2	23.1364	23.124	0.05	22.2293	22.2645	0.16	20.8814	20.9052	0.11	19.6866	19.5979	0.45	18.2463	18.0185	1.25
5	20.2245	20.0437	0.89	19.6779	19.5228	0.79	18.9023	18.739	0.86	18.2458	18.0185	1.25	17.4212	17.1211	1.72

Table 2. Non-dimensional mode 1 frequency of the SSSS 2D-FGM plate.

m_x	0.3			0.5			1			2			5		
m_y	Ref. [22]	Present	% Diff.	Ref. [22]	Present	% Diff.	Ref. [22]	Present	% Diff.	Ref. [22]	Present	% Diff.	Ref. [22]	Present	% Diff.
0.3	16.6028	15.957	3.89	15.9088	15.2332	4.25	14.5737	13.9133	4.53	12.904	12.3224	4.51	10.9331	10.4643	4.29
0.5	15.9088	15.2332	4.25	15.3087	14.63	4.43	14.1336	13.4864	4.58	12.6298	12.0572	4.53	10.8085	10.3417	4.32
1	14.5737	13.9133	4.53	14.1336	13.4864	4.58	13.241	12.63	4.61	12.0478	11.4981	4.56	10.5333	10.0727	4.37
2	12.904	12.3224	4.51	12.6298	12.0572	4.53	12.0478	11.4981	4.56	11.2284	10.7177	4.55	10.1272	9.6787	4.43
5	10.9331	10.4643	4.29	10.8085	10.3417	4.32	10.5333	10.0727	4.37	10.1272	9.6787	4.43	9.5452	9.1207	4.45

4.2. PTO of homogeneous isotropic plate

Before investigating the topology optimization behavior of bi-directional functionally graded plates, a validation example is first considered for a homogeneous isotropic plate. The purpose of this example is to verify the RPIM-PTO framework against previously published results in a standard benchmark setting.

In this example, the topology optimization of a square plate with side length $a = 1$ unit, subjected to a concentrated load of magnitude $F = 1$ unit applied at its center, is investigated. The applied load acts normal to the plate mid-surface. Two types of boundary conditions are considered, namely, plates with all four edges simply supported (SSSS) and plates with all four edges clamped (CCCC). Two uniform thickness ratios are examined: $h = a/100$, representing a thin plate, and $h = a/10$, corresponding to a thick plate. The material is characterized by a Young's modulus of $E_0 = 4$ unit and a Poisson's ratio of 0.3. Owing to geometric and loading symmetry, only one quarter of the plate is modeled. This computational domain is discretized using $n_x \times n_y = 41 \times 41$ scattered nodes, and 6400 design variables corresponding to integration points. For the optimization procedure, the penalization factor is taken as $p = 3$, the filter radius is specified as $r_0 = 2.0(a/n_x)$, and the prescribed volume fraction is 0.5.

Fig. 2 (a), (c) present the compliance convergence histories for the SSSS plates with thickness ratios of $h = a/100$ and $h = a/10$, respectively. The corresponding optimized topologies are displayed in Fig. 2 (b), (d), where the black regions represent the material retained after the optimization process. Fig. 3 (a), (c) present the compliance convergence histories for the CCCC plate, and the corresponding optimized topologies are displayed in Fig. 3 (b), (d).

The resulting material layouts are consistent with those reported in Refs. [20, 23, 24], thereby confirming the accuracy of the RPIM-PTO approach for the topology optimization of TSDT plates.

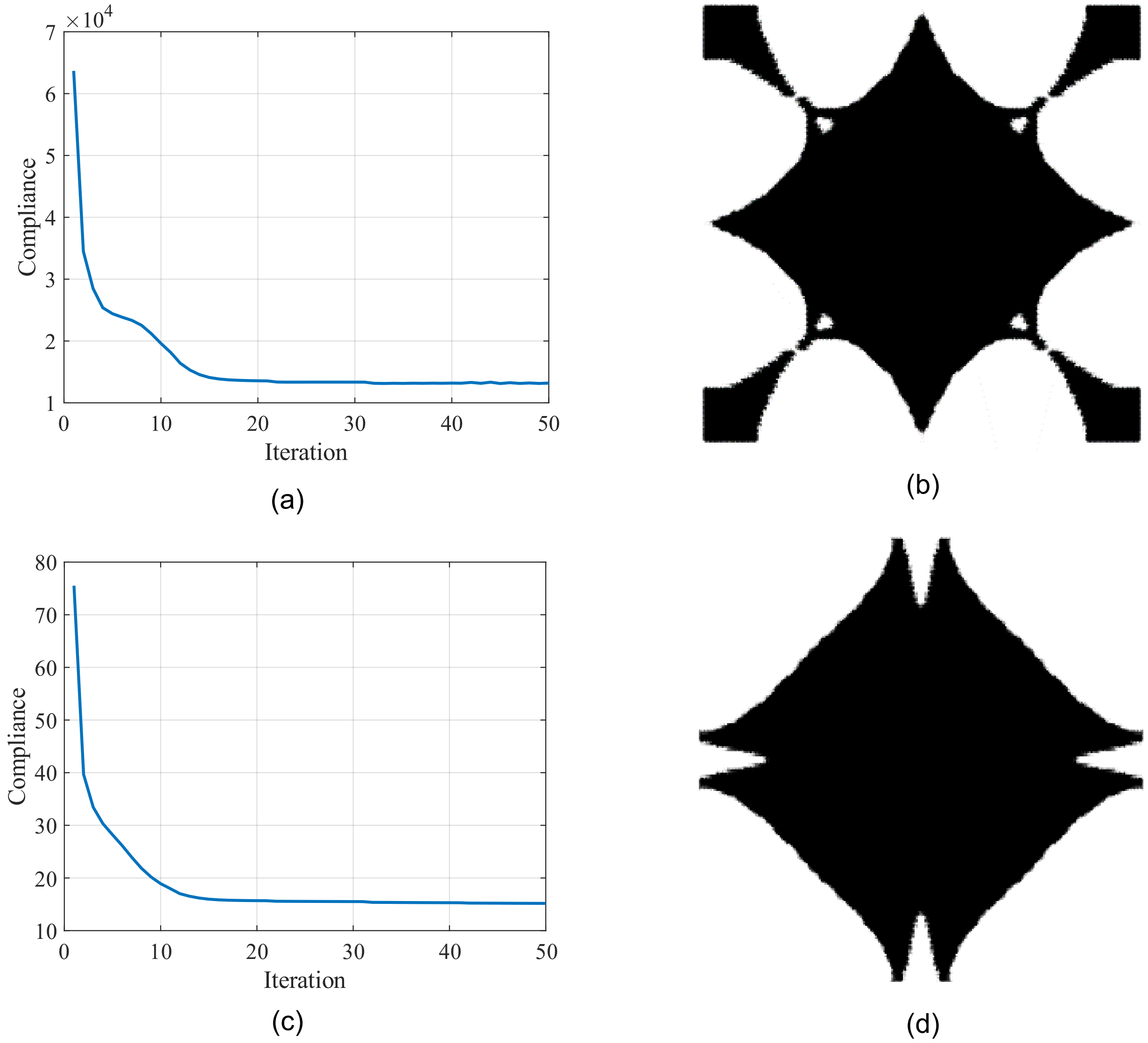

Fig. 2. Optimized thin and thick simply supported plate: (a) convergence of compliance in thin plate, (b) optimized material distribution in thin plate, (c) convergence of compliance in thick plate, and (d) optimized material distribution in thick plate.

5. Numerical examples

5.1. Problem description

This numerical example examines the influence of material gradation parameters, specifically m_x and m_y, on the optimized topology of a functionally graded plate. The geometry and boundary conditions of the problem are illustrated in Fig. 4. A uniformly distributed load of magnitude p = 1 unit is applied along two orthogonal lines, with one intersecting pass through the center of the plate. The square plate has dimensions $L_x = L_y = 100$ units, with two thickness scenarios considered: h = 10 units and h = 1 unit. The bidirectional functionally graded material is characterized by a Poisson's ratio v = 0.3, and a Young's modulus ratio of E_2/E_1 = 10, selected to enhance visual contrast in the color mapping of material distribution. A total of nine parametric cases are investigated, corresponding to combinations of m_x, m_y = [0.5, 1, 5]. The initial spatial distribution of material properties across the design domain is presented in Fig. 5.

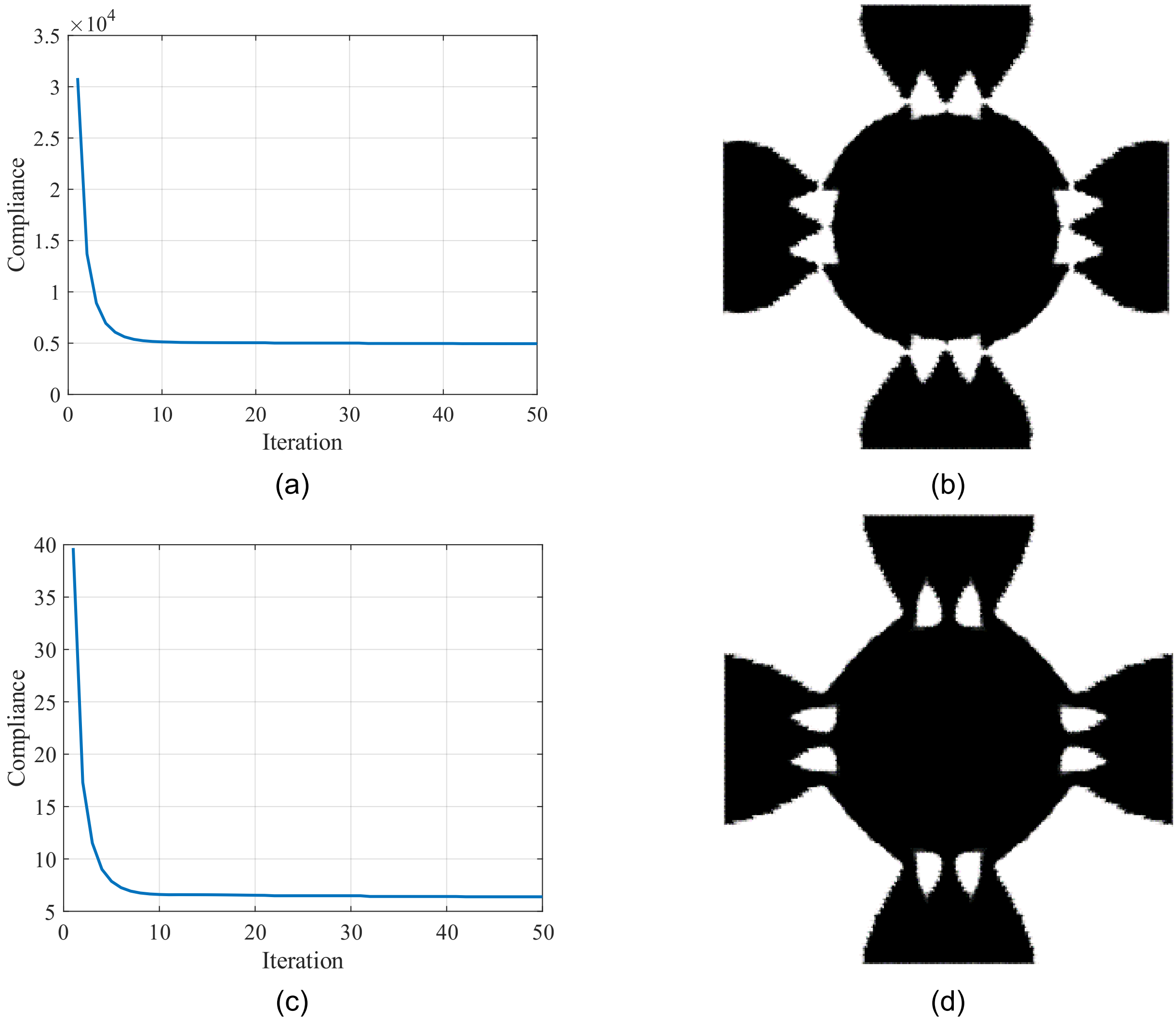

Fig. 3. Optimized thin and thick fully clamped plate: (a) convergence of compliance in thin plate, (b) optimized material distribution in thin plate, (c) convergence of compliance in thick plate, and (d) optimized material distribution in thick plate.

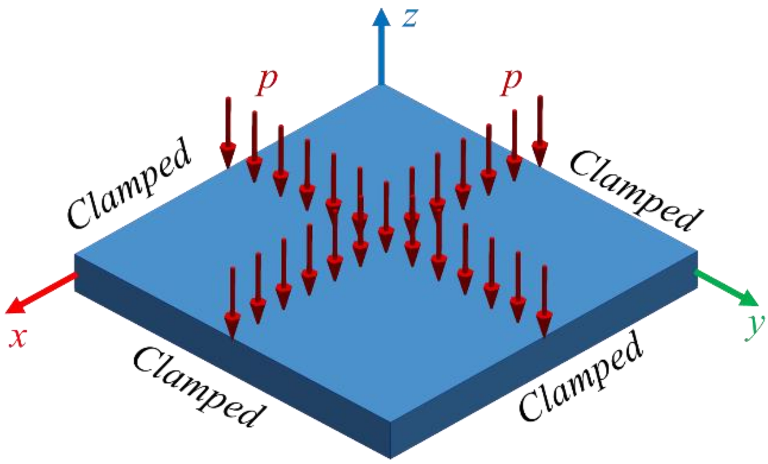

Fig. 4. Problem model, loads, and boundary conditions.

The design domain is discretized using a 51×51 nodal grid, resulting in 22500 design variables corresponding to integration points. A volume constraint of *f* = 50% is imposed to limit the total material usage. The radii of the support domain and density filter are set to 2.2 and 1.8 times the average nodal spacing, respectively. The choice of a relatively smaller filter is intended to reduce excessive smoothening in the optimized topology. In this study, no projection function is applied. A penalization factor of p = 3 is adopted for the SIMP interpolation, while the proportional coefficient α used in the material redistribution process is set to 0.5.

m_x = 0.5 m_x = 1 m_x = 5

m_y = 0.5

m_y = 1

m_y = 5

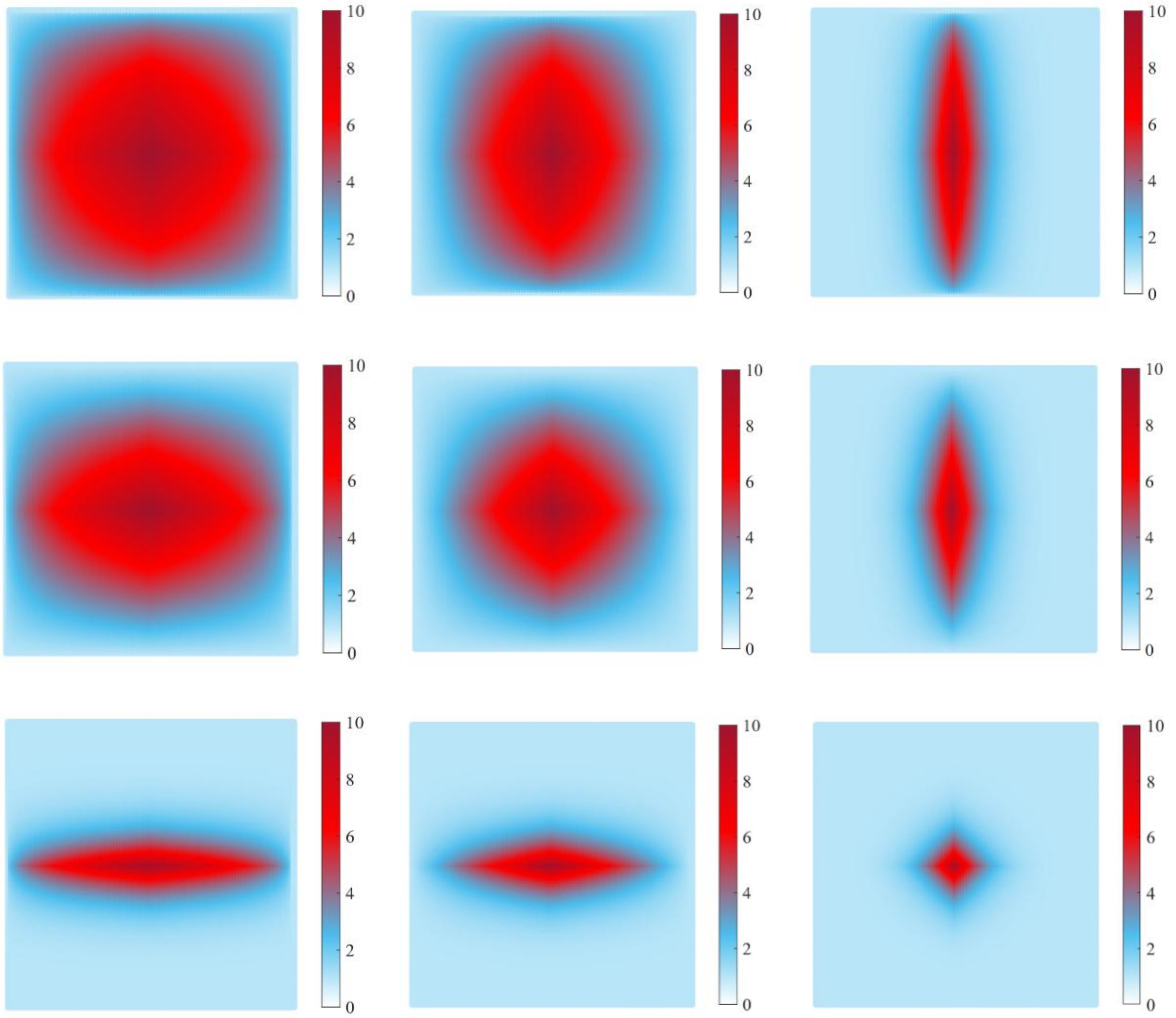

Fig. 5. Young's modulus distribution in the square design domain. The color bar indicates the E2/E1 ratio.

In Eq. (14), which defines the distribution of the material phases in the 2D functionally graded plate, the domain dimensions L_x and L_y appear explicitly in the expression for computing the volume fractions V_x and V_y. However, during the topology optimization process, the material layout evolves and the resulting configuration may no longer retain the original square geometry of the initial design domain. To maintain consistency and simplify the formulation, it is assumed that L_x and L_y remain unchanged and equal to the original dimensions of the square plate. Conceptually, this can be interpreted as extracting a subregion from an initially square functionally graded material plate, while preserving the underlying spatial distribution of material phases.

5.2. Results and discussion

Fig. 6 presents the optimized topologies of the h = 10 units plate along with their corresponding compliance values. As previously assumed, the spatial distribution of material phases remains unchanged from that shown in Fig. 5. From left to right and top to bottom in Fig. 6, a clear trend is observed: the compliance c increases progressively. Specifically, the configuration with m_x = m_y = 0.5 yields the lowest compliance, indicating the highest structural stiffness, whereas the case with m_x = m_y = 5 results in the highest compliance and thus the lowest stiffness. This observation is consistent with the underlying material phase distributions, where the m_x = m_y = 0.5 case exhibits a greater concentration of high-stiffness material (depicted in red and dark red) compared to the m_x = m_y = 5 case. Additionally, the compliance results exhibit symmetry, reflecting the symmetry of the material gradation parameters in both directions.

A similar trend is observed for the case with L_x/h = 100, as illustrated in Fig. 7. The compliance values exhibit symmetry, and increase consistently with higher values of the material gradation parameters m_x and m_y.

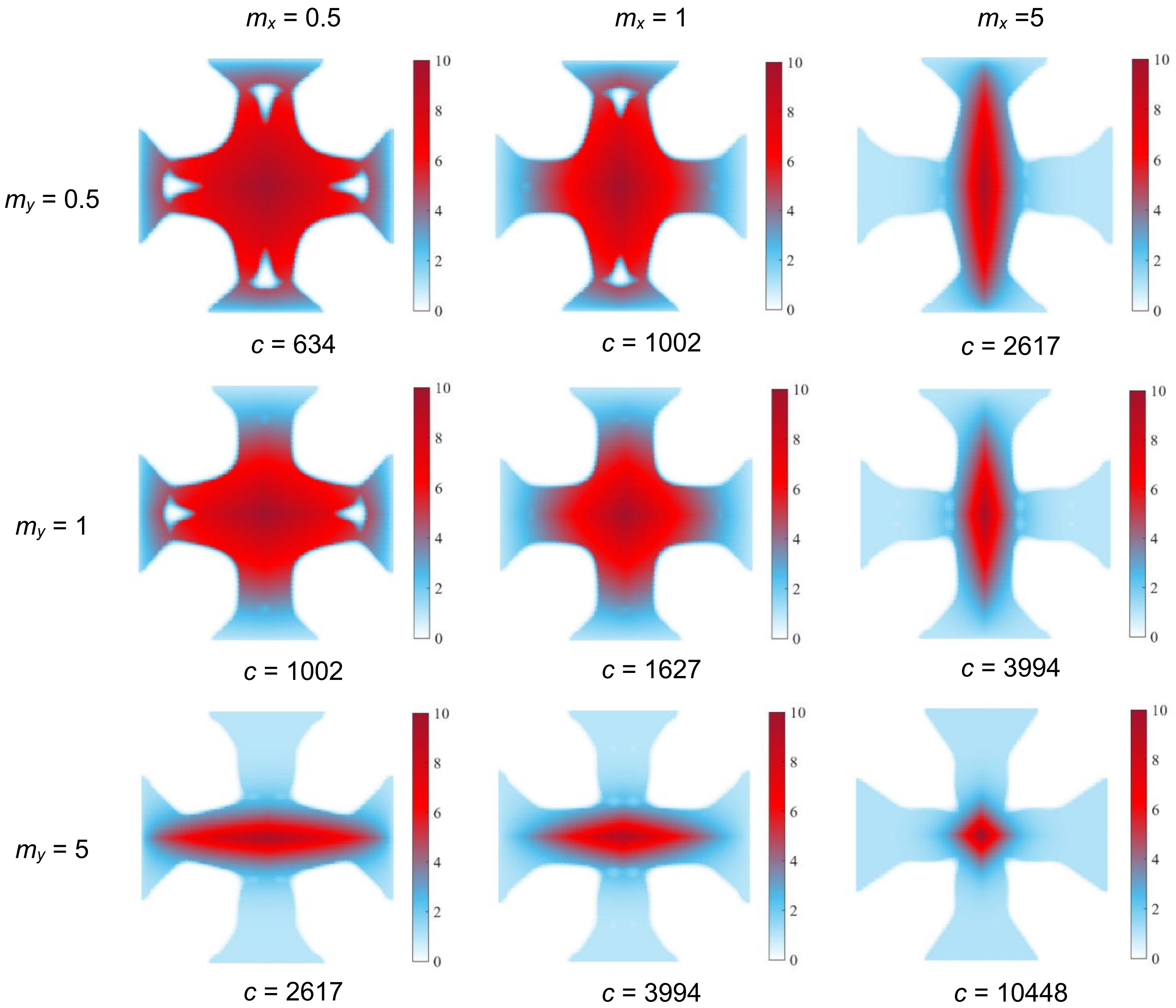

Fig. 6. Optimized configuration of the fully clamped plate (L_x/h = 10) with different m_x and m_y indices. The color bar indicates the E_2/E_1 ratio.

An important observation from the results in Fig. 6 and Fig. 7 is the presence of blurred or smeared regions around small-sized holes and narrow structural connections. This blurring effect arises from the application of the density filtering technique without incorporating a projection scheme to sharpen the boundaries of the optimized topology. The implementation of projection methods to enhance the clarity of the material layout is identified as a direction for future work.

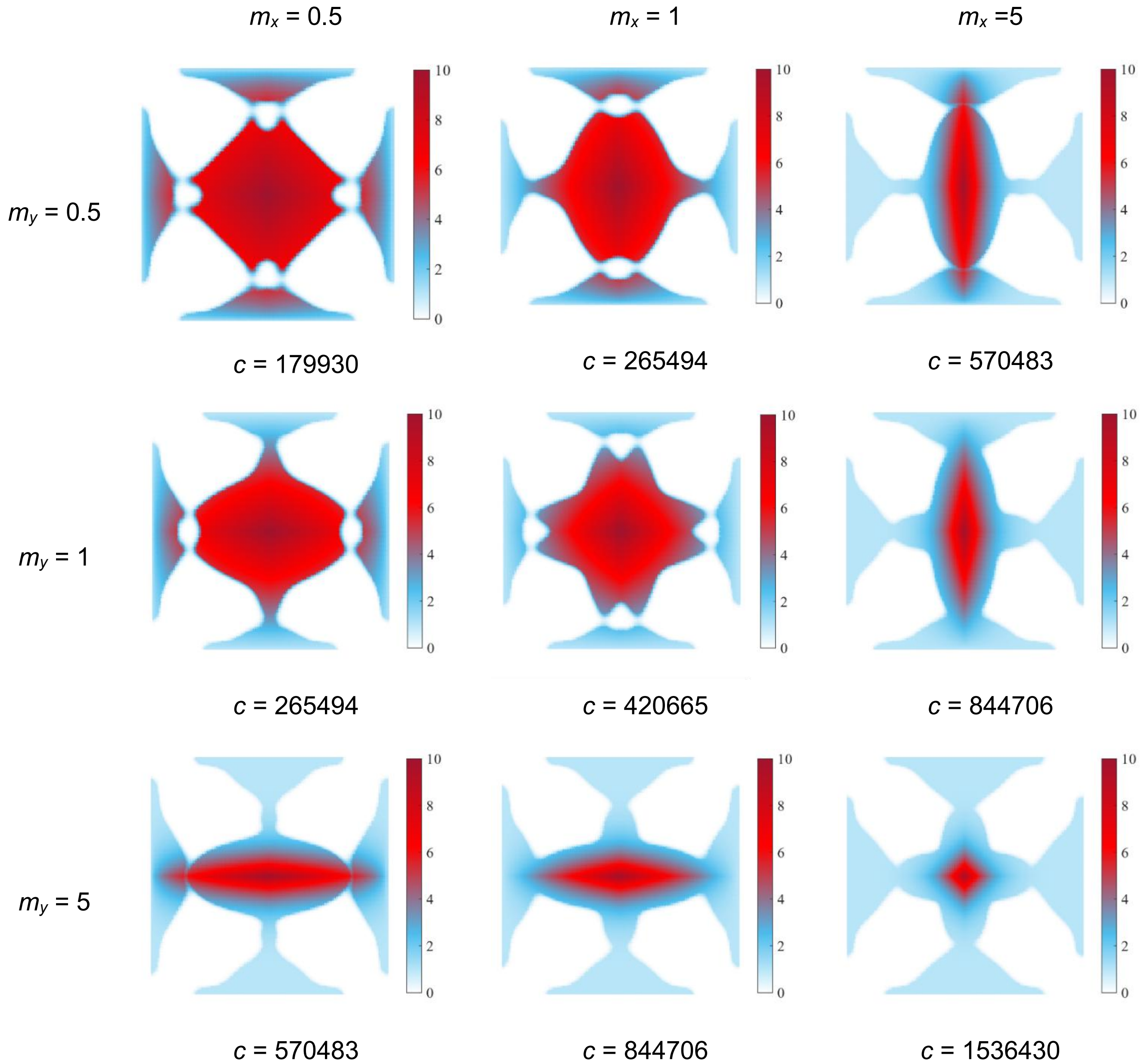

Fig. 7. Optimized configuration of the fully clamped plate (L_x/h = 100) with different m_x and m_y indices. The color bar indicates the E_2/E_1 ratio.

6. Conclusion

This study presents a meshfree framework for the topology optimization of plates composed of bi-directional functionally graded materials, employing third-order shear deformation theory for structural modeling. The radial point interpolation method is utilized as the numerical discretization scheme. A non-gradient-based optimization algorithm (proportional topology optimization) is adopted to iteratively update the material distribution. The numerical investigation considers multiple cases of material phase distributions characterized by different gradation indices in the *x*- and *y*-directions. A key assumption in the formulation is that the spatial variation of material phases remains unchanged during the optimization process. The results reveal symmetric trends in compliance with respect to the interchange of the material indices m_x and m_y, and demonstrate that structural compliance increases as these indices grow. This observation highlights the significant impact of material gradation on the resulting stiffness and topology.

Despite these promising results, the study is subject to limitations. Notably, the resolution of small-scale features is affected by the use of density filters without projection techniques, leading to blurred boundaries in regions of fine structural detail. Addressing this limitation by incorporating projection methods will be a focus of future research to enhance the optimized topologies.

Acknowledgments

This research is funded by Vietnam National University Ho Chi Minh City (VNU-HCM) under grant number C2025-20-01. We acknowledge Ho Chi Minh City University of Technology (HCMUT), VNU-HCM for supporting this study.

Declaration of Generative AI

During the preparation of this work, the authors used Claude in order to improve the readability and language of the manuscript. After using this tool, the authors reviewed and edited the content as needed and take full responsibility for the content of the published article.

References

[1] O. Sigmund. (2001). A 99 line topology optimization code written in Matlab. *Structural and Multidisciplinary Optimization*, 21, 120–127. https://doi.org/10.1007/s001580050176

[2] O.M. Querin, G.P. Steven, Y.M. Xie. (1998). Evolutionary structural optimisation (ESO) using a bidirectional algorithm. *Engineering Computations*, 15(8), 1031–1048. https://doi.org/10.1108/02644409810244129

[3] M.Y. Wang, X. Wang, D. Guo. (2003). A level set method for structural topology optimization. *Computer Methods in Applied Mechanics and Engineering*, 192(1–2), 227–246. https://doi.org/10.1016/S0045-7825(02)00559-5

[4] A. Takezawa, S. Nishiwaki, M. Kitamura. (2010). Shape and topology optimization based on the phase field method and sensitivity analysis. *Journal of Computational Physics*, 229(7), 2697–2718. https://doi.org/10.1016/j.jcp.2009.12.017

[5] E. Andreassen, A. Clausen, M. Schevenels, B.S. Lazarov, O. Sigmund. (2011). Efficient topology optimization in MATLAB using 88 lines of code. *Structural and Multidisciplinary Optimization*, 43, 1–16. https://doi.org/10.1007/s00158-010-0594-7

[6] E. Biyikli, A.C. To. (2015). Proportional Topology Optimization: A new Non-Sensitivity method for solving stress constrained and minimum compliance problems and its implementation in MATLAB. *PLoS ONE*, 10(12), e0145041. https://doi.org/10.1371/journal.pone.0145041

[7] G.R. Liu. (2009). Meshfree Methods: Moving Beyond the Finite Element Method, Second Edition (2nd ed.). *CRC Press*. https://doi.org/10.1201/9781420082104

[8] M. Cui, H. Chen, J. Zhou, F. Wang. (2017). A meshless method for multi-material topology optimization based on the alternating active-phase algorithm. *Engineering With Computers*, 33, 871–884. https://doi.org/10.1007/s00366-017-0503-4

[9] J. Zhang, S. Wang, G. Zhou, S. Gong, S. Yin. (2020). Topology optimization of thermal structure for isotropic and anisotropic materials using the element-free Galerkin method. *Engineering Optimization*, 52(7), 1097–1118. https://doi.org/10.1080/0305215X.2019.1636979

[10] T.T. Truong, V.S. Lo, N.T. Nguyen, M.N. Nguyen. (2021). Free Vibration Analysis Of Cracked Kirchhoff-Love Plate Using The Extended Radial Point Interpolation Method. *Vietnam Journal of Science and Technology*, 59(6). https://doi.org/10.15625/2525-2518/59/6/15953

[11] V.S. Lo, T.T. Truong, N.T. Nguyen. (2023). Dynamic analysis of cracked plates based on a first-order shear deformation theory formulation by using an extended meshfree method. *IOP*

Conference Series: Materials Science and Engineering, 1289(1), 012003. https://doi.org/10.1088/1757-899X/1289/1/012003

[12] J.N. Reddy. (1984). A simple Higher-Order theory for laminated composite plates. *Journal of Applied Mechanics*, 51(4), 745–752. https://doi.org/10.1115/1.3167719

[13] C. Wang, L. Ma, Y. Bu, J. Zhao, K.H. Cheong. (2023). Multi-patch isogeometric material optimization of bi-directional functionally graded plates. *Composite Structures*, 326, 117584. https://doi.org/10.1016/j.compstruct.2023.117584

[14] L. Ma, C. Wang, Y. Chong, W. Hu, L. Zeng. (2024). Isogeometric material optimization for shape control of bi-directional functionally graded plates with piezoelectric layers. *Thin-Walled Structures*, 202, 112067. https://doi.org/10.1016/j.tws.2024.112067

[15] F.J. Ramírez-Gil, E.C.N. Silva, W. Montealegre-Rubio. (2024). Design of topology-optimized functionally graded porous structures under transient loads. *International Journal of Mechanical Sciences*, 284, 109732. https://doi.org/10.1016/j.ijmecsci.2024.109732

[16] I. Khan, Z. Ullah, B. Ullah, Siraj-Ul-Islam, W. Khan. (2025). Stress-based topology optimization using maximum entropy basis functions-based meshless method. *Engineering With Computers*, 41, 1721–1745. https://doi.org/10.1007/s00366-024-02047-2

[17] A. Joglekar, H. Chen, L.B. Kara. (2024). DMF-TONN: Direct Mesh-free Topology Optimization using Neural Networks. *Engineering With Computers*, 40, 2227–2240. https://doi.org/10.1007/s00366-023-01904-w

[18] S. Ren, C. Cheng, B. Yu, Z. Meng, B. Huang, Q. Wu. (2022). New refined higher-order shear deformation theories for functionally graded plates conforming to graded variations of material properties. *European Journal of Mechanics - a/Solids*, 94, 104621. https://doi.org/10.1016/j.euromechsol.2022.104621

[19] M.N. Nguyen, T.Q. Bui. (2022). A meshfree-based topology optimization approach without calculation of sensitivity. *Vietnam Journal of Mechanics*, 44(1), 45–58. https://doi.org/10.15625/0866-7136/16679

[20] M.N. Nguyen, T.Q. Bui. (2022). Multi-material gradient-free proportional topology optimization analysis for plates with variable thickness. *Structural and Multidisciplinary Optimization*, 65, 75. https://doi.org/10.1007/s00158-022-03176-2

[21] S.J. Lee, J.N. Reddy, F. Rostam-Abadi. (2004). Transient analysis of laminated composite plates with embedded smart-material layers. *Finite Elements in Analysis and Design*, 40(5–6), 463–483. https://doi.org/10.1016/S0168-874X(03)00073-8

[22] X. Chen, Y. Lu, Z. Wu, Y. Shao, X. Xue, Y. Wu. (2023). Free vibration of in-plane bi-directional functionally graded materials rectangular plates with geometric imperfections and general elastic restraints. *Aerospace Science and Technology*, 132, 108045. https://doi.org/10.1016/j.ast.2022.108045

[23] Q.H. Pham, D. H. Phan. (2022). Polygonal topology optimization for Reissner–Mindlin plates. *Engineering with Computers.* 38, 141–154. https://doi.org/10.1007/s00366-020-01047-2

[24] Cui T., Sun Z., Liu C., Li L., Cui R., Guo X. (2020). Topology optimization of plate structures using plate element-based moving morphable component (MMC) approach. *Acta Mech. Sin.* 36, 412–421. https://doi.org/10.1007/s10409-020-00944-5